ACS POLYMERS Au
AN OPEN ACCESS JOURNAL OF THE AMERICAN CHEMICAL SOCIETY

pubs.acs.org/polymerau
Article

Pattern Formation in Evaporating Polymer Solutions—Interplay between Dewetting and Decomposition

Published as part of ACS Polymers Au virtual special issue "Polymer Science and Engineering in India".

Pankaj Mahawar,[§] M. Praveena,[§] Shreyanil Bhuyan, Dipin S. Pillai, and Sivasurender Chandran*

Cite This: *ACS Polym. Au* 2024, 4, 302−310

ABSTRACT: Pattern formation during solution evaporation is common in several industrial settings and involves a complex interplay of multiple processes, including wetting/dewetting, diffusion, and rheological characteristics of the solution. Monitoring the emergence of patterns during evaporation under controlled conditions may allow deconvolution of different processes and, in turn, improve our understanding of this common yet complex phenomenon. Here, we probe the importance of initial conditions, defined by the solution concentration c_0, on the pattern formation in evaporating polymer solutions on the air−water interface. Intriguingly, the initial decrease in the lateral length scale (ξ), characterizing the patterns, takes an upturn at higher concentrations, revealing reentrant behavior. We employ a gradient dynamics model consisting of coupled evolution equations for the film height and the polymer fraction in the solution. Our simulations capture two different length scales revealing the reasons underlying the re-entrant behavior of $\xi(c_0)$. While the long-range destabilizing interactions between suspension and water result in the dewetting of thin film solutions, the phase separation between the polymer and solvent occurs at shorter length scales. Our results demonstrate the importance of initial concentration on pattern formation and, thereby, on the resultant properties of thin polymer films.

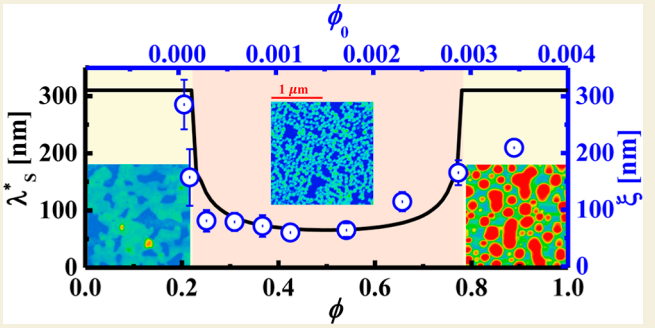

KEYWORDS: *pattern formation, dewetting, evaporation, Langmuir polymer films, gradient dynamics model, linear stability analysis, nonlinear dynamics simulations*

INTRODUCTION

Pattern formation during the evaporation of suspensions is a common and recurring phenomenon. As an example, we often observe ring-like patterns formed by the evaporation of spilled-over suspensions like coffee, inks, or paints.[1−3] Several industrial applications like large-scale coating,[4,5] fabrication of solar cells,[6] inkjet printing,[7] disease detection,[8] and forensic investigation of blood droplets[9] rely on the understanding of such evaporation-induced patterns. Further, the evaporation of solutions containing one or more components provides an avenue to control pattern formation across several length scales.[10−19] Despite its enormous practical potential, the complex interplay of several physicochemical processes during evaporation limits our ability to fully harness evaporation to control pattern formation.[11,20−22]

Evaporation is inherently a nonequilibrium process. The fraction of solutes in an initially dilute suspension progressively increases, resulting in variations in their flow behavior, which, in turn, could affect the wetting/dewetting rate and diffusion of solutes.[4,11,20,21] Evaporation may create local concentration fluctuations, resulting in phase transitions like crystallization[11,23,24] and glass transition.[4,25−27] In addition, the interaction of the suspension with the substrate dictates the contact line dynamics and thus reflects on the resulting patterns.[28,29] To understand the development of evaporation-induced patterns, several theoretical approaches involving hydrodynamics and contact line dynamics,[30−32] gradient dynamics with lubrication approximation,[33−35] and moving boundary models were developed.[36−38] However, despite such progress, a complete understanding of the mechanisms underlying the pattern formation of evaporating solutions remains elusive.

Here, we probe the importance of initial conditions, defined by the solution concentration (c_0), on pattern formation in

Received: March 9, 2024
Revised: April 25, 2024
Accepted: April 26, 2024
Published: May 13, 2024

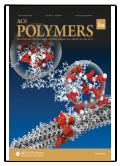

https://doi.org/10.1021/acspolymersau.4c00018
ACS Polym. Au 2024, 4, 302−310

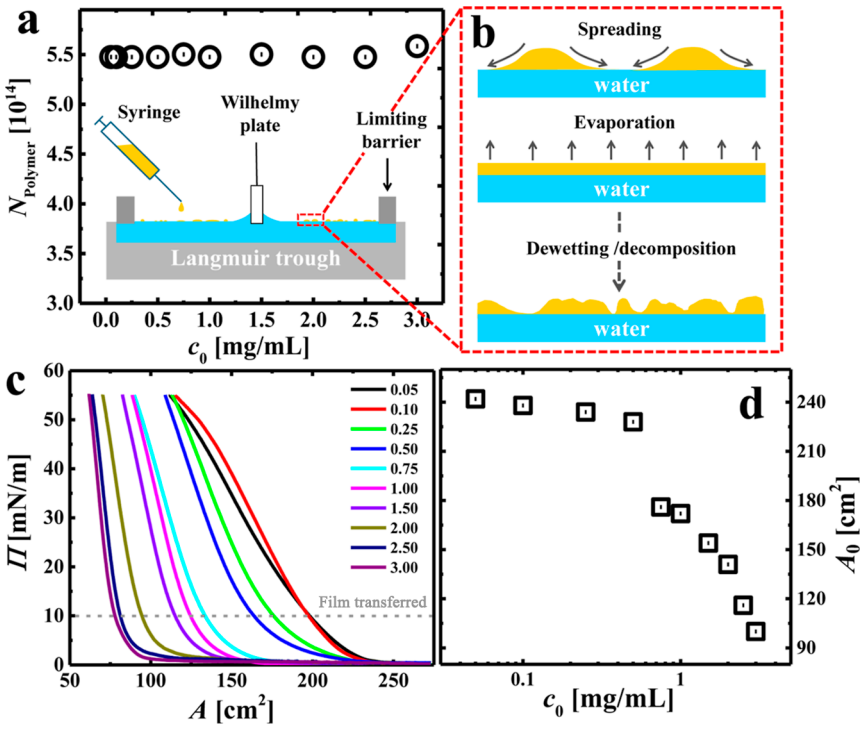

Figure 1. Role of initial concentration on film characteristics: (a) the number ($N_{polymer}$) of polymers spread on the water surface is shown as a function of the initial concentration c_0 with an appropriately adjusted volume. (b) Schematic representation of the key stages involved in the evaporation of the polystyrene solution on the water surface. (c) Surface pressure isotherms, Π vs A, for films formed from solutions of different c_0 as defined in the panel in the units of mg/mL. The horizontal dashed line at Π = 10 mN/m highlights the pressure at which films are transferred. (d) Limiting area, A_0, as a function of c_0.

evaporating polymer solutions. For a systematic control, we rely on a Langmuir trough, which allows the probing of the characteristics of the patterns before transferring the dried layers to a solid substrate. The dried films exhibit patterns such as flat islands with holes in between, networks, and domains, suggesting the dewetting of polymer solutions at the air−water interface. The initially constant film height (h_m) increases monotonically with c_0 beyond a critical concentration c_c. Intriguingly, we observe that the lateral length scale (ξ), characterizing the patterns, displays a re-entrant behavior, i.e., the initial decrease in ξ takes an upturn at higher concentrations. We employ a gradient dynamics model consisting of coupled evolution equations for the height and polymer fraction in the suspension film. Our careful simulations, complemented by linear stability analysis, capture the growth of two different length scales in a narrow intermediate concentration range, while the low- and high-concentration suspensions exhibit the growth of a single length scale. While the long-range destabilizing interactions between suspension and water result in the dewetting of thin film solutions, the phase separation between the polymer and solvent occurs at shorter length scales. Nonlinear simulations revealed that decomposition, despite its lower growth rate, may nonlinearly dominate pattern formation at the intermediate concentrations. The change in $\xi(c_0)$ across the re-entrant behavior quantitatively agrees with our minimal model. Our results demonstrate that the initial concentration of the suspensions serves as a unique lever for quantitative control of the evaporation-induced patterns. Such explicit control over pattern formation would allow the tuning of various physical properties of polymer films.[4,5,10]

EXPERIMENTAL SECTION

Materials

We used thiol-terminated polystyrene with molecular weight M_w = 11 kg/mol and $Đ$ = 1.04, as purchased from Sigma-Aldrich. For dissolving polystyrene molecules, we used high-purity (≈99.8%) chloroform. We used deionized Milli-Q water with a resistivity of 18 MΩcm as a subphase in the Langmuir trough (Biolin Scientific). A Hamilton syringe with a capacity of 50 μL (purchased from Hamilton, Romania) was used to spread the polymer suspension onto the air−water interface. Polymer films as prepared were transferred onto a coverslip (received from Blue Star, India) sized at 22 × 22 mm^2.

Methods

Substrate Preparation. Glass coverslips were cleaned using the RCA method to remove residual organic contamination and particles from the surface.[39] Here, we briefly describe the procedure. A solution containing a 1:1:5 mixture of ammonium hydroxide (NH_4OH), hydrogen peroxide (H_2O_2), and deionized water (H_2O) was heated to a temperature of *ca.* 75 °C. Coverslips were immersed in this solution for 30 min and subsequently rinsed with plenty of deionized water. Such freshly treated surfaces were purged in dry nitrogen to ensure the complete evaporation of water.

Langmuir Technique. For all our experiments, we employed a Langmuir trough with a maximum surface area of 273 cm^2. The temperature of the trough was maintained at *ca.* 25 °C. The entire system was enclosed within a closed chamber to prevent environmental contamination and minimize perturbation due to acoustic vibrations. Surface pressure is defined as $\Pi = \gamma_0 - \gamma$, where γ_0 stands for the surface tension of ultrapure Milli-Q water, and γ is the effective surface tension of the layer, which is proportional to the surface concentration of polymers. We utilized a platinum plate as the Wilhelmy plate for measuring Π. We used homogeneous solutions of polystyrene in chloroform with various concentrations ranging from 0.05 to 3 mg/mL. To ensure homogeneous dissolution, we stirred the solutions overnight. Chloroform facilitated the spreading of solution

https://doi.org/10.1021/acspolymersau.4c00018
ACS Polym. Au 2024, 4, 302−310

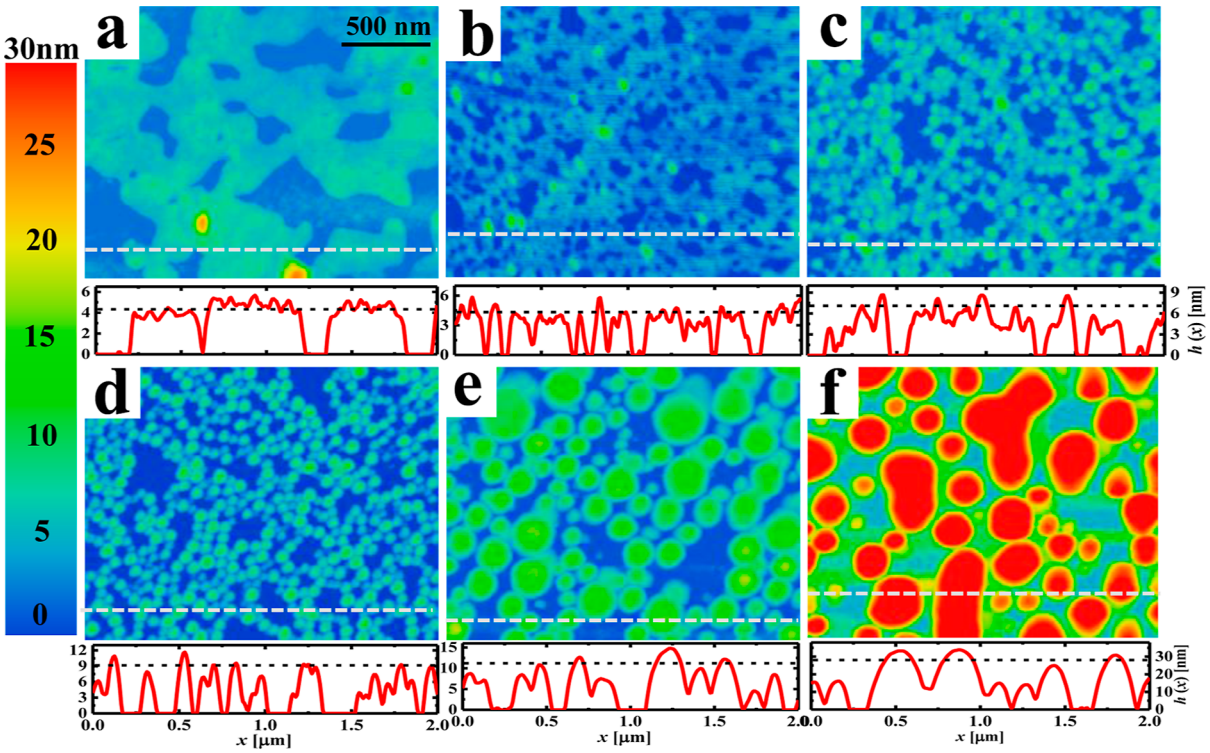

Figure 2. Evaporation-induced pattern formation—role of initial concentration: representative surface morphologies of polystyrene films prepared from solutions with different initial concentrations: (a) c_0 = 0.05 mg/mL, (b) c_0 = 0.25 mg/mL, (c) c_0 = 0.75 mg/mL, (d) c_0 = 1.00 mg/mL, (e) c_0 = 2.00 mg/mL, and (f) c_0 = 3.00 mg/mL, respectively. Height profiles $h(x)$ corresponding to the dashed lines in the images are shown below each micrograph. The dashed lines shown in $h(x)$ vs x indicate the mean height (h_m) of the patterns.

on the air−water interface due to its low boiling point and low surface tension. Using a Hamilton syringe, we spread the solutions drop-by-drop at various locations on the water surface. The total spreading volume was appropriately adjusted to maintain a constant total number of polymers for all of the experiments. The surface pressure was monitored closely while spreading. Newer drops were spread only after the fluctuations in surface pressure caused by the earlier drop completely relaxed to zero. We waited for at least 15 min after spreading to ensure a complete evaporation of the solvent. The floating polymer layers were compressed gently at a rate of 5 mm/min to avoid compression-induced instabilities and other artifacts at the surface. Surface pressure isotherms were recorded by plotting Π as a function of area A between the limiting barriers. To capture the patterns as they are formed, we transferred the films from the water surface to freshly cleaned glass coverslips using the Langmuir−Blodgett (LB) deposition method. To ensure optimal coverage and to avoid compression-induced pattern formation, we transferred all films at a minimal surface pressure Π = 10 mN/m.[15] The substrates were lifted at a rate of 5 mm/min while simultaneously compressing at the same rate. This allowed us to minimize transfer-induced artifacts in the patterns. The deposited polymer films were completely dried by using a vacuum desiccator at ambient temperature.

Atomic Force Microscopy and Image Analysis. Surface morphology of the dried polymer films was probed by atomic force microscopy (AFM) in tapping (or semicontact) mode, using Origin MFP+3D (Oxford Instruments, UK). A cantilever with a resonance frequency of *ca.* 70 kHz, a force constant of 1.7 N/m, and a radius of curvature of *ca.* 7 nm was used for our measurements. We used a minimal normal force to avoid force-induced deformations. For a free oscillation voltage of 1 V, we typically used a set-point of *ca.* 0.7 V. The scanning rates were limited to 0.5 and 1 Hz to prevent scan instabilities and the dragging of the tip on the sample surface. Scanning was conducted at room temperature within a sealed chamber to mitigate contamination and to minimize acoustic vibrations. Image scanning was conducted at various locations across the polymer films, excluding the edges of the sample, to ensure that no artifacts resulting from LB transfer methods are inadvertently captured. The raw data were flattened using Gwyddion software.[40] All images are presented as obtained without any additional processing. The resultant images are depicted with an appropriate color bar according to the height distribution of the patterns.

EXPERIMENTAL RESULTS

Evaporation of Solutions with Different Initial Concentrations

The crucial aspect of evaporation-induced pattern formation is the spreading of polymer solutions at the air−water interface. The mobility of the underlying water surface avoids the pinning of the three-phase contact line of the droplets and hence allows homogeneous spreading on the surface. In our experiments, we systematically vary the initial solution concentrations c_0 but fix the total number $N_{polymer}$ of polymers by appropriately varying the volume of the solution spread on the water surface (see Figure 1a). The initial rate of spreading on the water surface results from a balance of the driving capillary and the resisting viscous forces,[41,42] along with simultaneous evaporation. To understand this interplay between spreading and evaporation, it is instructive to compare the rates of both processes. For the initial dilute concentrations, the spreading rate is largely dominated by interactions between the solvent chloroform and the interface. Recent experiments reveal that chloroform evaporates at a rate of $v_{ev} \approx 0.1\ \mu$m/s.[43] Using the values for the spreading parameter ($|S| \approx 10^{-2}$ N/m), contact angle ($\theta \approx 0.1$), and viscosity ($\eta \approx 10^{-3}$ Pa.s) from the literature,[43] we obtain the initial spreading velocity,[42] $v_{spread} \sim |S|\cdot\theta^2/\eta$, to be of the order of cm/s. Of course, any presence of convective flow of air at the air−water interface may increase the evaporation rate considerably. However, our experiments performed in an enclosed cabinet ensure negligible effects of airflow on evaporation. Therefore, in the initial stages of solution spreading, $v_{ev} \ll v_{spread}$ suggests the domination of spreading over evaporation. Therefore, as captured in Figure 1b, we may

https://doi.org/10.1021/acspolymersau.4c00018
ACS Polym. Au 2024, 4, 302−310

conceive that the polymer solution undergoes an immediate transition from its initial drop-like shape to that of a flat thin film before any considerable evaporation can occur. Thereafter, with the evaporation of the solvent molecules, we expect a progressive increase in the concentration of polymers, and the spreading behavior will eventually be driven by the characteristics of the polymer, here polystyrene. The spreading parameter for polystyrene on water is negative.[43,44] Thus, at later stages, we expect a complete dewetting of the thin film solution (Figure 1b). With an increase in the initial concentration, assuming a monotonic change in the spreading parameter, one may expect monotonic variation in the dewetting length scale. However, given that the number of molecules is held constant and that we have a mobile surface, do changes in the initial concentration reflect in pattern formation?

To answer this, we employ the water subphase of a Langmuir trough as the substrate for spreading polystyrene solutions at different initial concentrations. The Langmuir technique offers several advantages that make it an ideal experimental system for addressing this question: (a) the ability to gather the dewetted domains across the water surface together via the moving mechanical barriers, (b) the ability to characterize the nature of patterns and the evolution of mechanical interactions between them via surface pressure isotherms, and (c) the possibility of transferring the patterns onto solid substrates for further investigation. After spreading the solutions, we provided sufficient time to ensure complete evaporation of the solvent. Upon complete evaporation, dry dewetted polymer layers float on the surface. Such layers are compressed together to obtain surface pressure isotherms, as summarized in Figure 1c. All systems exhibit a range of area A, with no detectable surface pressure ($\Pi \approx 0$), revealing an incomplete coverage of the dewetted patterns. With compression, i.e., on reducing the area between the barriers, Π increases monotonically, reflecting the interaction between the dewetted patterns. In line with earlier reports, we use a minimal compression rate (5 mm/min) to avoid compression-induced artifacts on the patterns.[15] Interestingly, though $N_{polymer}$ is constant for all solutions, the area A_0 below which Π increases varies sensitively with the initial concentration c_0 of the solution. We quantify this observation in Figure 1d by plotting A_0 as a function of c_0. There is an apparent decrease in A_0 with an increase in c_0, suggesting concentration-induced differences in the patterns floating on the water surface. We may attribute the decrease in A_0 to the loosely packed patterns and/or the presence of thicker clusters with increasing c_0. To understand this further, it is important to probe the patterns formed on the water surface. For this purpose, we transfer the patterns onto a solid surface at a minimal pressure Π = 10 mN/m to ensure that the compression has a negligible role in the self-assembled structures.[15] The patterns as transferred are dried overnight in a vacuum to remove any traces of water. After appropriate drying, all films are investigated with an atomic force microscope.

Initial Concentration Affects Evaporation-Induced Patterns

We summarize the role of initial concentration in pattern formation in Figures 2, 3, and 4. As captured in Figure 2a, we observe flat structures with holes in between for c_0 = 0.05 mg/mL. With an increase in c_0 to 0.25 mg/mL, we notice an increased density of smaller holes (Figure 2b). On increasing c_0 to 0.75 mg/mL, as captured in Figure 2c, we observe networks with underlying domain-like structures. With a further increase in $c_0 \geq 1$ mg/mL, domain-like patterns with an increasing lateral length scale and height are observed. At first glance, it is tempting to relate the concentration-induced differences in the patterns to the patterns frozen after different durations of dewetting.[45] Dewetting of the film on an unfavorable surface is initiated by the rupture of the film to create holes that grow with time. Such growing holes may eventually coalesce to form networks. Upon small perturbations, the Rayleigh–Plateau instability drives the liquid filaments contained in the network to form domains, which may coalesce further to form larger domains. Thus, with time, we may expect a sequence of patterns: (i) holes in films, (ii) a network of filaments, (iii) the emergence of domain-like structures within the networks, and (iv) completely decoupled domains. While this sequence appears similar to the concentration-dependent transitions in patterns, there are important differences that need further attention. For instance, there is a rapid increase in the height of the patterns for concentrations $c_0 \geq 0.75$ mg/mL. In addition, the uniformity of the features in c_0 = 0.25 mg/mL and c_0 = 0.75 mg/mL suggest the presence of instabilities like spinodal dewetting.[46,47] To further understand this behavior, we quantify the patterns via two prominent length scales: the mean height h_m of the patterns and the lateral length scales ξ.

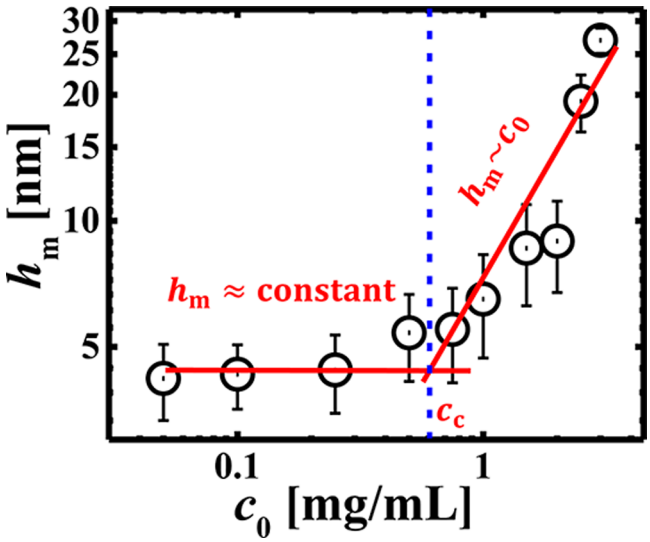

Figure 3. Evolution of the mean height of the patterns with initial concentration: double logarithmic representation of the mean height h_m (open symbols) of the patterns as a function c_0. The solid red lines trace the concentration dependence of $h_m \approx$ constant for $c_0 < c_c$ and $h_m \sim c_0$ for $c_0 > c_c$. The vertical dashed line marks the value of the critical concentration c_c.

Let us begin with a discussion of the height of the patterns. Representative height profiles corresponding to all the images are shown in Figure 2. We observe a systematic increase in the height of the patterns with an increase in c_0. As shown in Figure 3, we quantify this by plotting the mean height h_m of the structures as a function of c_0. Initially, for all concentrations $c_0 < c_c$ = 0.6 mg/mL, the mean height $h_m \approx$ 4 nm does not exhibit any dependence on concentration c_0. We use polystyrene chains of molecular weight, M_w = 11 kDa, i.e., with the number of monomers $N \approx 106$. Using Kuhn length of a_k = 0.67 nm, we obtain the end-to-end distance of the chain $R_{ee} = a_k \cdot \sqrt{N} \approx 6.9$ nm and radius of gyration $R_g = \frac{R_{ee}}{\sqrt{6}} \approx 2.8$ nm under melt conditions.[48] Thus, $h_m \approx$ 4 nm for $c_0 < c_c$ reveals that the patterns formed are of polystyrene monolayers. For all initial concentrations $c_0 > c_c$, we observe $h_m \sim c_0$. This is along the expected lines as the height of resulting layers ought to be proportional to the initial concentration.[27,49]

To characterize the lateral length scales defining the pattern, we rely on the power spectral density (PSD) analysis of the images. As captured in Figure 4a, we observe a transition from PSD $\sim k^0$ for $k < k_c$ to PSD $\sim k^{-4}$ for $k > k_c$, where k_c defines a crossover wave vector. This crossover from a constant PSD to a power law decrease is similar to that of the transition from Guinier to Porod behavior in the form factor considered in scattering.[50,51] The wave vector independence of the PSD at low k is due to the finite size effects, and the power law decrease (PSD $\sim k^{-4}$) beyond a critical wave vector k_c is because of the smooth surface of the scattering entities, here the patterns.[50] Thus, the crossover wave vector allows us to capture the largest lateral correlation length scales, $\xi = 2\pi/k_c$, defining the patterns. The crossover wave vector, k_c, displays an intriguing dependence on the initial concentration. While k_c for the lowest and the highest

https://doi.org/10.1021/acspolymersau.4c00018
ACS Polym. Au 2024, 4, 302−310

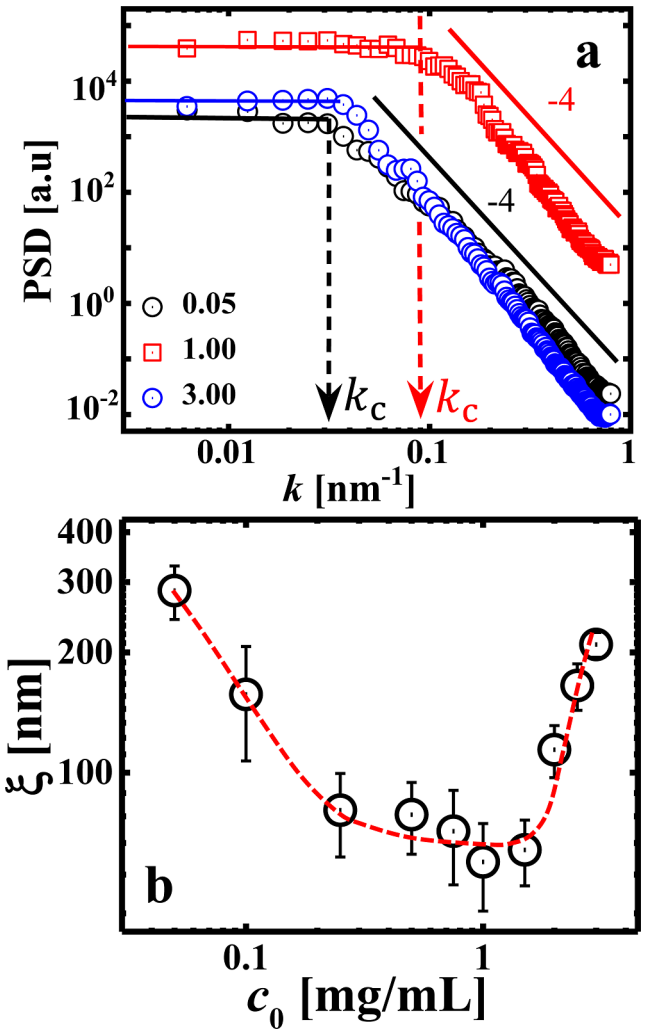

Figure 4. Re-entrant transition in lateral length scales with initial concentration: (a) double logarithmic representation of the power spectral densities (PSDs) as a function of wave vector k. Data are shown for films formed from solutions of different c_0 represented in the legend in units of mg/mL. The vertical dashed arrows point to the crossover wave vector, $k = k_c$, capturing the transition from constant Guinier (k^0) to Porod (k^{-4}) behavior. (b) Double logarithmic representation of the largest lateral length scales $\xi = 2\pi/k_c$ as a function of c_0. The dashed line is a guide to the eyes.

concentrations are similar, k_c for intermediate concentrations is higher. This suggests a re-entrant transition in the lateral length scales with concentration. In Figure 4b, we plot ξ as a function of c_0 for all the suspensions. For all concentrations, $c_0 < c_c$, ξ decreases systematically from *ca.* 300 nm down to *ca.* 70 nm. However, for $c_0 > c_c$, ξ takes an upturn and increases with an increase in c_0 to a maximum of *ca.* 220 nm. We observe a clear re-entrant behavior of ξ with an increase in c_0. How do we understand this re-entrant behavior of $\xi(c_0)$?

Recent experiments on polymer-grafted nanoparticles revealed such re-entrant transition in lateral length scales.[15] Supporting simulations based on the gradient dynamics model revealed that the bimodality corresponds to dewetting and concentration decomposition mediated by the interplay of enthalpic and entropic interactions.[15] However, these simulations predicted that the length scales corresponding to these instabilities vary by more than 2 orders of magnitude.[15,34] In our experiments, the maximum difference in length scales is only a factor of 3−4. While qualitatively, our experiments show similar reentrant behavior, the actual length scales differed by orders of magnitude. Thus, to understand the re-entrant behavior, we develop a minimal model inspired by the gradient dynamics model of Thiele and co-workers.[15,33,34]

THEORETICAL MODELING

Model Description

Several recent works have demonstrated the effectiveness of the gradient dynamics model in capturing the instabilities in thin films of solutions or suspensions.[33,34,52] As established in the previous section, the initial film spreading occurs with negligible evaporation and results in a flat film at the air−water interface. The evolution of such a thin film can be described using gradient dynamics for the conserved fields, i.e., the film height $h(x, t)$ and the local amount of solute $\psi(x, t) = h(x, t)\phi(x, t)$, where $\phi(x, t)$ is the volume fraction of the polymer. The effective free energy of the polymer solution thin film is thus a functional of the film height $h(x, t)$ and the local amount of solute $\psi(x, t)$. The free energy functional, $F[h,\psi]$, is given by[52]

$$F[h, \psi] = \int \left[\gamma\left(1 + \frac{1}{2}|\nabla h|^2\right) + f(h) + hG(\phi) + \sigma\frac{h|\nabla\phi|^2}{2} \right] dA \quad (1)$$

Here, γ is the surface tension of the solutions, and σ is the interfacial stiffness. The first term in eq 1 defines the free surface energy. The second term in eq 1 is the dewetting potential describing long-range destabilizing forces between the solution film and the substrate. This potential is defined as

$$f(h) = \frac{A_H}{6\pi h_e^2}\left(-\frac{h_e}{h} + \frac{h_e^2}{2h^2}\right) \quad (2)$$

where A_H is the Hamaker constant and h_e is the equilibrium height that minimizes the dewetting potential. The third term in eq 1 signifies the bulk interaction potential capturing the possible concentration-dependent phase separation between polymer and solvent. Motivated by the Cahn−Hilliard theory of decomposition,[53] we use a double well potential of the form $\sim (\phi(\phi - 1))^2$. Scaling this double well form with the energy density, we obtain

$$G(\phi) = B\frac{k_B T}{a^3}(\phi(\phi - 1))^2 \quad (3)$$

Here, k_B is the Boltzmann constant, T is the temperature of the system, and a is the molecular size. The measure of the strength of the interaction, B, is tuned to match the experimental conditions. Unlike earlier works,[15,34] we neglect the contribution of the conformational entropy of the chains in the interaction potential due to the short chain length present in our system. The last term in eq 1 defines the energetic penalty due to concentration gradients.

The temporal evolution of the coupled conserved fields, $h(x, t)$ and $\psi(x, t)$, is related to the spatial gradients of the variational derivative of the free energy functional $F[h,\psi]$ as[34]

$$\frac{\partial h}{\partial t} = \nabla\cdot\left(Q_{hh}\nabla\frac{\delta F}{\delta h} + Q_{h\psi}\nabla\frac{\delta F}{\delta \psi}\right) \quad (4)$$

$$\frac{\partial \psi}{\partial t} = \nabla\cdot\left(Q_{\psi h}\nabla\frac{\delta F}{\delta h} + Q_{\psi\psi}\nabla\frac{\delta F}{\delta \psi}\right) \quad (5)$$

https://doi.org/10.1021/acspolymersau.4c00018
ACS Polym. Au 2024, 4, 302−310

Here, $\frac{\delta F}{\delta h}$ and $\frac{\delta F}{\delta \psi}$ are the variational derivatives of energy functional F with respect to h and ψ, respectively. In the above, Q_{hh}, $Q_{h\psi}$, $Q_{\psi h}$, and $Q_{\psi\psi}$ are the mobility factors and the element of the mobility matrix, Q, which is defined as follows

$$Q = \begin{pmatrix} Q_{hh} & Q_{h\psi} \\ Q_{\psi h} & Q_{\psi\psi} \end{pmatrix} = \frac{1}{3\eta}\begin{pmatrix} h^3 & h^2\psi \\ h^2\psi & h\psi^2 + \frac{a^2}{2\pi}\psi \end{pmatrix} \quad (6)$$

Linear Stability Analysis

To obtain insights into the resultant length scales, we rely on a linear stability analysis. This method evaluates the stability of a spatially uniform base state through modal analysis, wherein it is subjected to a periodic perturbation characterized by a wave vector, k. The system is considered unstable when it deviates from its base state upon perturbation, and the rate of this deviation is quantified by the growth rate (β). The wave vector (k_{max}) at which the growth rate reaches its maximum value determines the characteristic length scale of pattern formation.[54] The wavelength, which is also the characteristic length scale, is computed as λ_{max} ($=2\pi/k_{max}$). We obtain the solutions by perturbing the initially constant film height and volume fraction in the modal form as

$$h(x, t) = \overline{h} + \epsilon\tilde{h}e^{ikx+\beta t} \quad (7)$$

$$\psi(x, t) = \overline{\psi} + \epsilon\tilde{\psi}e^{ikx+\beta t} \quad (8)$$

The governing equation is nondimensionalized using appropriate scales, and the variables h and ψ are, respectively, perturbed about their base states $\overline{h}$ and $\overline{\psi}$ ($=\overline{h}\overline{\phi}$) with extremely small amplitudes $\epsilon\tilde{h}$ and $\epsilon\tilde{\psi}$ as shown in eqs 7 and 8. Here, $\epsilon \ll 1$.

A set of two linear equations in $\tilde{h}$ and $\tilde{\psi}$ is obtained by linearizing the governing eqs 4 and 5 as follows

$$\beta\tilde{h} = E_{11}\tilde{h} + E_{12}\tilde{\psi} \quad \text{and} \quad \beta\tilde{\psi} = E_{21}\tilde{h} + E_{22}\tilde{\psi} \quad (9)$$

This system of linear equations can be converted to a 2×2 matrix eigenvalue problem with E_{11}, E_{12}, E_{21}, and E_{22} as its elements. All these elements are functions of the wave vector (k). The eigenvalues of this matrix are computed to determine the growth rate (β). Owing to a two-dimensional matrix, two eigenvalues are obtained. For a given k, we obtain two real eigenvalues β, and the maximum of these is taken as the growth rate corresponding to k. The sign of β determines the stability of the system; a negative value implies that the system is stable, while a positive value implies that the system is unstable. From this analysis, we obtain the dispersion relation, i.e., the dependence of growth rate (β) on wave vector (k).

The values of the parameters used for the analysis are as follows: $A_H = 2 \times 10^{-17}$ Nm, $\overline{h} = 30$ nm, $\overline{\phi} = 0.6$, $h_e = 0.1\overline{h}$, $a = 1$ nm, $\gamma = 27.15$ mN/m, $\eta = 0.0025$ Pa·s, $\sigma = a\gamma$, $B = 0.12$, $T = 300$ K, and $k_B = 1.38 \times 10^{-23}$ J/K. The vertical characteristic length scale $l = 10$ nm, the lateral length scale $L = l^2\sqrt{\frac{6\pi\gamma}{A_H}}$, and the time scale $t_0 = \frac{6\pi\eta l L^2}{A_H}$.

Theoretical Results: Linear Stability Analysis

The results of the linear stability analysis are summarized in Figure 5. The dispersion curves corresponding to different polymer fractions are shown in Figure 5a. At extreme polymer fractions, $\phi < 0.23$ and $\phi > 0.77$, we observe a single maximum in the dispersion curve suggesting the presence of a single mode of instability with wavelength $\lambda_1 = 2\pi/k_1$. However, for all intermediate polymer fractions $0.23 < \phi < 0.77$, we observe additional local maxima at higher wavevectors k_2, suggesting the presence of another mode of instability with a smaller wavelength $\lambda_2 = 2\pi/k_2$. To highlight this observation, in Figure 5b, we display the concentration dependence of characteristic wavelengths λ_1 and λ_2. Thus, our linear stability analysis captures two different modes for intermediate polymer fractions. It is promising to note that the values of λ_1 and λ_2 are similar to the values of ξ shown in Figure 4b. However, the reasons underlying these instabilities need further discussion.

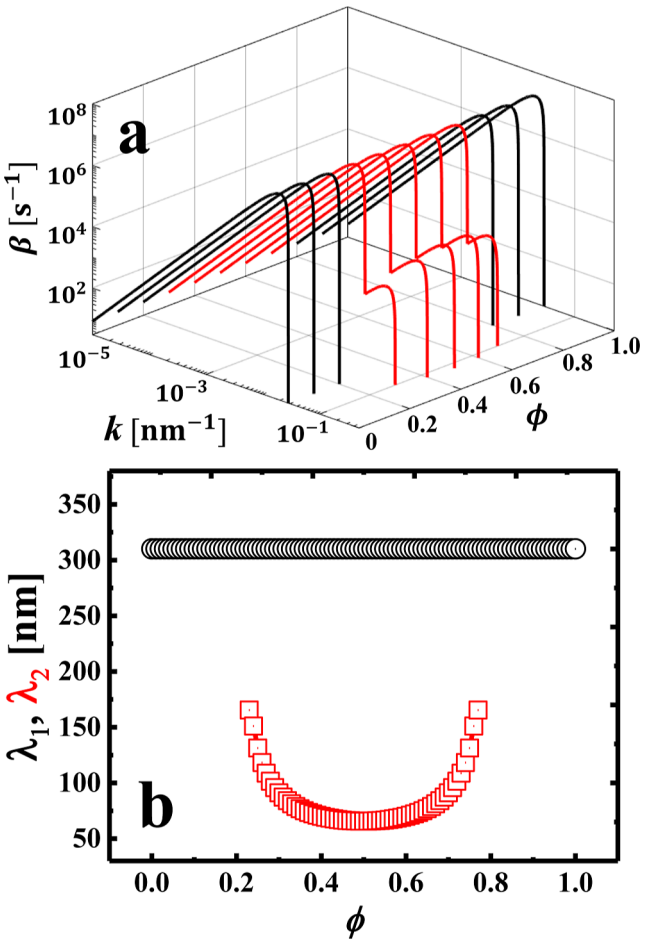

Figure 5. Linear stability analysis capturing two modes of instabilities: (a) double logarithmic representation of the dispersion curves, growth rate β as a function of wavevector k, for solutions containing different volume fractions (ϕ) of polymer. While the lower and higher fractions of the polymer exhibit a single mode k_1, intermediate fractions (red continuous lines) reveal an additional mode k_2. (b) The concentration dependence of the corresponding length scales, $\lambda_1 = 2\pi/k_1$ and $\lambda_2 = 2\pi/k_2$, of these instabilities is shown.

Theoretical Results: Nonlinear Simulations

To understand the reason underlying the two modes of instability, we performed nonlinear simulations probing the spatiotemporal evolution of the two conserved variables h and ψ. As discussed earlier, we infinitesimally perturb the initially flat film, as given by eqs 7 and 8. For this simulation, we considered domain sizes that are integral multiples of the characteristic wavelengths, λ_1 and λ_2. To begin, we consider a

https://doi.org/10.1021/acspolymersau.4c00018
ACS Polym. Au 2024, 4, 302−310

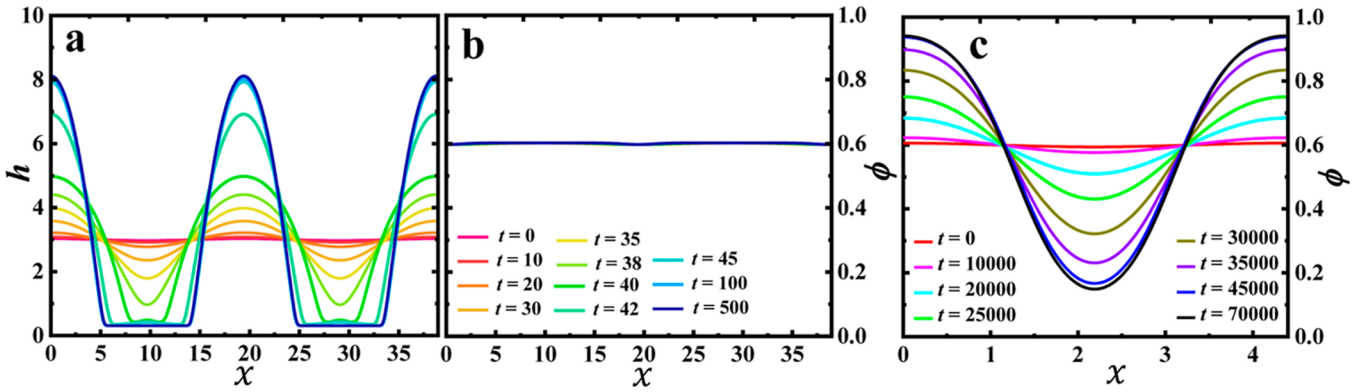

Figure 6. Nonlinear simulation capturing dewetting and decomposition: spatiotemporal evolution of (a) the nondimensional height profile, $h(x, t)$, and (b) the volume fraction profile, $\phi(x, t)$, within a computational domain length of $2\lambda_1$. Different lines correspond to simulation runs for different times, as defined in panel (b). (c) Long-time simulations capturing the evolution of polymer fraction, ϕ, in a computational domain length of λ_2 despite its low growth rate. For nondimensionalizing the variables, we use a lateral length scale, L = 16 nm, and a vertical length scale, l = 10 nm, and the time scale t_0 = 6 ns.

domain size of $2\lambda_1$. No flow conditions are imposed at the boundaries, and periodic sinusoidal perturbations with a small amplitude (1%) are imposed as initial conditions. The finite difference method with 2000 regularly spaced grid points is employed to solve the differential equations, which was verified to be sufficient to obtain grid-independent solutions. The simulated spatiotemporal profiles of the film height (h) and the volume fraction of the polymer (ϕ) are shown in Figure 6. We observe a systematic evolution of $h(x, t)$ (Figure 6a), while $\phi(x, t)$ is approximately constant (Figure 6b). This observation suggests that this corresponds to the dewetting instability of the thin film solution. The fact that the periodicity of $h(x)$ matches exactly with λ_1 reveals that λ_1 captures the length scale corresponding to the dewetting mode. The results shown in Figure 6a,b capture solely the dewetting mode. How about the other instability corresponding to λ_2? Because of the lower growth rate β corresponding to the second mode, we run the simulations for a longer time to allow for the manifestation of the mode corresponding to λ_2. To reduce the computational cost, a domain size equal to λ_2 is chosen. For this smaller domain size, 1000 grid points were chosen for the simulation. Clearly, for longer simulation runs, the polymer fraction evolves with time without much variations in h, suggesting an instability corresponding to concentration decomposition. The periodicity of $\phi(x)$, a shown in Figure 6c, is the same as that of λ_2, revealing that the second mode of instability, observed at intermediate polymer fractions, corresponds to concentration decomposition.

Corroboration of Experiments and Simulations

As summarized in the previous section, simulations capture the coexistence of dewetting and decomposition instabilities for all intermediate polymer fractions. Interestingly, although the growth rates of decomposition modes are significantly smaller than that of the dewetting mode, our nonlinear simulations revealed the development of concentration decomposition for long waiting times. Thus, we define a single length scale $\lambda_s^* = \lambda_2$ for all intermediate fractions ($0.23 < \phi < 0.77$) and $\lambda_s^* = \lambda_1$ for $\phi < 0.23$ and $\phi > 0.77$ capturing the dominant length scale in simulations. The concentration dependence of λ_s^* is shown in Figure 7. Also shown is the experimental measure of the lateral length scales ξ as a function of the initial volume fraction (ϕ_0) of polymers in the solution. At this point, it is important to highlight the differences between the experimental initial fraction of polymers ϕ_0 and the fraction of polymers ϕ used in the simulations. Experimentally, ϕ_0 characterizes the initial concentration of the solution. However, one can conceive that the dewetting or decomposition will initiate at later stages of evaporation, where the actual fraction of polymers would certainly be significantly higher than that of ϕ_0. Unlike in experiments, the polymer fraction ϕ used in simulations is the fraction at which the instabilities occur. Thus, the differences observed between the experimental and theoretical intermediate fractions are expected. We may improve the situation by incorporating a sink term in the coupled evolution equations.[55,56] The time dependence of the sink term could capture the effect of evaporation, which, in turn, may allow us to use the same definition for the concentration in both experiments and simulations. Despite the apparent differences, our simplified simulations impressively capture the experimental re-entrant behavior of $\xi(\phi_0)$ by $\lambda_s^*(\phi)$. Thus, a concentration-dependent transition from dewetting to decomposition and eventually to

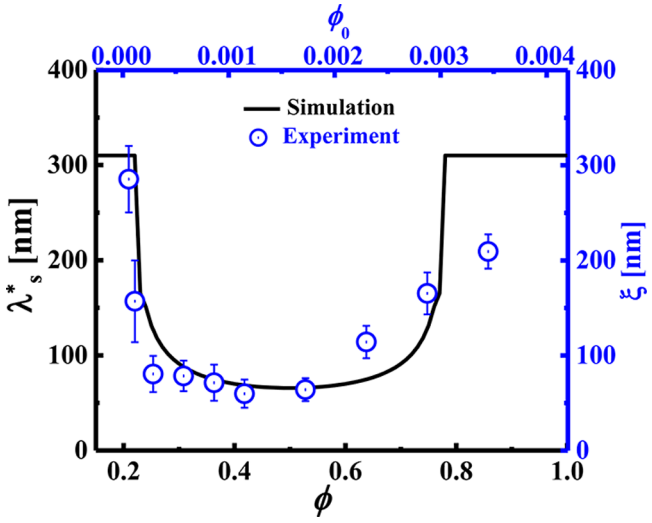

Figure 7. Corroboration between experiments and simulations: quantitative agreement between experiments, ξ vs ϕ_0, and simulations λ_s^* vs ϕ. The extent of re-entrant in ξ is well captured by λ_s^* with the fraction of polymers.

https://doi.org/10.1021/acspolymersau.4c00018
ACS Polym. Au 2024, 4, 302−310

dewetting underlies the observation of the re-entrant behavior of $\xi(\phi_0)$.

CONCLUSIONS

In conclusion, we have demonstrated the importance of initial conditions, defined via the initial concentration, on the length scale ξ characterizing the evaporation-induced patterns in thin polymer solutions. We reveal an intriguing concentration-dependent re-entrant behavior in the lateral length scales defining the patterns. Despite the simplifications of our model, we demonstrate that our simulation results are in quantitative agreement with the experimental results. Such a good corroboration allows us to reveal that the re-entrant behavior of $\xi(\phi_0)$ is driven by the interplay of two instabilities: dewetting and decomposition. Our work provides an avenue to harness evaporation protocols to obtain hierarchical self-assembled patterns of polymers. Such differences in patterns would allow control over the resultant physical properties of polymer films.

AUTHOR INFORMATION

Corresponding Author

Sivasurender Chandran − *Soft and Biological Matter Laboratory, Department of Physics, Indian Institute of Technology Kanpur, Kanpur 208016, India;* orcid.org/0000-0003-0547-0282; Email: schandran@iitk.ac.in

Authors

Pankaj Mahawar − *Soft and Biological Matter Laboratory, Department of Physics, Indian Institute of Technology Kanpur, Kanpur 208016, India*

M. Praveena − *Soft and Biological Matter Laboratory, Department of Physics, Indian Institute of Technology Kanpur, Kanpur 208016, India*

Shreyanil Bhuyan − *Department of Chemical Engineering, Indian Institute of Technology Kanpur, Kanpur 208016, India*

Dipin S. Pillai − *Department of Chemical Engineering, Indian Institute of Technology Kanpur, Kanpur 208016, India;* orcid.org/0000-0002-7607-7923

Complete contact information is available at: https://pubs.acs.org/10.1021/acspolymersau.4c00018

Author Contributions

[§]P.M. and M.P. have equal contribution. CRediT: **Pankaj Mahawar** data curation, formal analysis, investigation, methodology, writing-original draft, writing-review & editing; **Mullapudi Praveena** data curation, formal analysis, investigation, methodology; **Shreyanil Bhuyan** formal analysis, methodology, validation, writing-original draft, writing-review & editing; **Dipin S. Pillai** formal analysis, funding acquisition, methodology, resources, supervision, writing-original draft, writing-review & editing; **Sivasurender Chandran** conceptualization, formal analysis, funding acquisition, project administration, resources, supervision, visualization, writing-original draft, writing-review & editing.

Notes

The authors declare no competing financial interest.

ACKNOWLEDGMENTS

We acknowledge the funding from the Startup Research Grant (SRG/2021/001276) and MATRICS grant (MTR/2022/000804), Science and Engineering Research Board. We acknowledge the Center for Nanosciences at IIT Kanpur for AFM measurements.

REFERENCES

(1) Deegan, R. D.; Bakajin, O.; Dupont, T. F.; Huber, G.; Nagel, S. R.; Witten, T. A. Capillary flow as the cause of ring stains from dried liquid drops. *Nature* **1997**, *389*, 827−829.

(2) Thampi, S. P.; Basavaraj, M. G. Drying Drops of Colloidal Dispersions. *Annu. Rev. Chem. Biomol. Eng.* **2023**, *14*, 53−83.

(3) Mampallil, D.; Eral, H. B. A review on suppression and utilization of the coffee-ring effect. *Adv. Colloid Interface Sci.* **2018**, *252*, 38−54.

(4) Chandran, S.; Baschnagel, J.; Cangialosi, D.; Fukao, K.; Glynos, E.; Janssen, L. M.; Muller, M.; Muthukumar, M.; Steiner, U.; Xu, J.; et al. Processing Pathways Decide Polymer Properties at the Molecular Level. *Macromolecules* **2019**, *52*, 7146−7156.

(5) Gu, X.; Shaw, L.; Gu, K.; Toney, M. F.; Bao, Z. The meniscus-guided deposition of semiconducting polymers. *Nat. Commun.* **2018**, *9*, 534.

(6) Saki, Z.; Byranvand, M. M.; Taghavinia, N.; Kedia, M.; Saliba, M. Solution-processed perovskite thin-films: the journey from lab-to large-scale solar cells. *Energy Environ. Sci.* **2021**, *14*, 5690−5722.

(7) de Gans, B.; Duineveld, P. C.; Schubert, U. S. Inkjet printing of polymers: state of the art and future developments. *Adv. Mater.* **2004**, *16*, 203−213.

(8) Rapis, E. A change in the physical state of a nonequilibrium blood plasma protein film in patients with carcinoma. *Technol. Phys.* **2002**, *47*, 510−512.

(9) Chen, R.; Zhang, L.; Zang, D.; Shen, W. Blood drop patterns: Formation and applications. *Adv. Colloid Interface Sci.* **2016**, *231*, 1−14.

(10) Müller, M.; Abetz, V. Nonequilibrium processes in polymer membrane formation: Theory and experiment. *Chem. Rev.* **2021**, *121*, 14189−14231.

(11) Zhou, J.; Man, X.; Jiang, Y.; Doi, M. Structure Formation in Soft-Matter Solutions Induced by Solvent Evaporation. *Adv. Mater.* **2017**, *29*, 1703769.

(12) Rabani, E.; Reichman, D. R.; Geissler, P. L.; Brus, L. E. Drying-mediated self-assembly of nanoparticles. *Nature* **2003**, *426*, 271−274.

(13) Kinge, S.; Crego-Calama, M.; Reinhoudt, D. N. Self-assembling nanoparticles at surfaces and interfaces. *ChemPhysChem* **2008**, *9*, 20−42.

(14) Huang, J.; Kim, F.; Tao, A. R.; Connor, S.; Yang, P. Spontaneous formation of nanoparticle stripe patterns through dewetting. *Nat. Mater.* **2005**, *4*, 896−900.

(15) Sarika, C.; Tomar, G.; Basu, J.; Thiele, U. Bimodality and re-entrant behaviour in the hierarchical self-assembly of polymeric nanoparticles. *Soft Matter* **2015**, *11*, 8975−8980.

(16) Bormashenko, E.; Pogreb, R.; Musin, A.; Stanevsky, O.; Bormashenko, Y.; Whyman, G.; Gendelman, O.; Barkay, Z. Self-assembly in evaporated polymer solutions: Influence of the solution concentration. *J. Colloid Interface Sci.* **2006**, *297*, 534−540.

(17) Bormashenko, E.; Pogreb, R.; Stanevsky, O.; Bormashenko, Y.; Stein, T.; Gaisin, V.-Z.; Cohen, R.; Gendelman, O. V. Mesoscopic patterning in thin polymer films formed under the fast dip-coating process. *Macromol. Mater. Eng.* **2005**, *290*, 114−121.

(18) Bormashenko, E.; Pogreb, R.; Stanevsky, O.; Bormashenko, Y.; Gendelman, O. Formation of honeycomb patterns in evaporated polymer solutions: Influence of the molecular weight. *Mater. Lett.* **2005**, *59*, 3553−3557.

(19) Tönsmann, M.; Scharfer, P.; Schabel, W. Critical solutal Marangoni number correlation for short-scale convective instabilities in drying poly (vinyl acetate)-methanol thin films. *Polymers* **2021**, *13*, 2955.

(20) Zang, D.; Tarafdar, S.; Tarasevich, Y. Y.; Dutta Choudhury, M.; Dutta, T. Evaporation of a Droplet: From physics to applications. *Phys. Rep.* **2019**, *804*, 1−56.
(21) Parsa, M.; Harmand, S.; Sefiane, K. Mechanisms of pattern formation from dried sessile drops. *Adv. Colloid Interface Sci.* **2018**, *254*, 22−47.
(22) Routh, A. F. Drying of thin colloidal films. *Rep. Prog. Phys.* **2013**, *76*, 046603.
(23) Park, M. S.; Aiyar, A.; Park, J. O.; Reichmanis, E.; Srinivasarao, M. Solvent evaporation induced liquid crystalline phase in poly (3-hexylthiophene). *J. Am. Chem. Soc.* **2011**, *133*, 7244−7247.
(24) Qian, Q.; Yu, S.; Li, C. Y. Tuning Poly (l-lactic acid) Crystallization Pathways via Evaporative Crystallization on a Water Surface. *Macromolecules* **2023**, *56*, 8747−8753.
(25) Peter, S.; Meyer, H.; Baschnagel, J. Molecular dynamics simulations of concentrated polymer solutions in thin film geometry. II. Solvent evaporation near the glass transition. *J. Chem. Phys.* **2009**, *131*, 014903.
(26) Rauch, J.; Köhler, W. Diffusion and thermal diffusion of semidilute to concentrated solutions of polystyrene in toluene in the vicinity of the glass transition. *Phys. Rev. Lett.* **2002**, *88*, 185901.
(27) Chandran, S.; Handa, R.; Kchaou, M.; Al Akhrass, S.; Semenov, A. N.; Reiter, G. Time allowed for equilibration quantifies the preparation induced nonequilibrium behavior of polymer films. *ACS Macro Lett.* **2017**, *6*, 1296−1300.
(28) Picknett, R.; Bexon, R. The evaporation of sessile or pendant drops in still air. *J. Colloid Interface Sci.* **1977**, *61*, 336−350.
(29) Sahoo, S.; Mukherjee, R. Pattern formation in evaporative drying of a polymer solution droplet over a soft swellable substrate. *Langmuir* **2023**, *39*, 9526−9537.
(30) Hu, H.; Larson, R. G. Evaporation of a sessile droplet on a substrate. *J. Phys. Chem. B* **2002**, *106*, 1334−1344.
(31) Larson, R. G. Instabilities in viscoelastic flows. *Rheol. Acta* **1992**, *31*, 213−263.
(32) Hu, H.; Larson, R. G. Marangoni effect reverses coffee-ring depositions. *J. Phys. Chem. B* **2006**, *110*, 7090−7094.
(33) Thiele, U.; Todorova, D. V.; Lopez, H. Gradient dynamics description for films of mixtures and suspensions: Dewetting triggered by coupled film height and concentration fluctuations. *Phys. Rev. Lett.* **2013**, *111*, 117801.
(34) Sarika, C.; Tomar, G.; Basu, J. Pattern formation in thin films of polymer solutions: Theory and simulations. *J. Chem. Phys.* **2016**, *144*, 024902.
(35) Clarke, N. Toward a model for pattern formation in ultrathin-film binary mixtures. *Macromolecules* **2005**, *38*, 6775−6778.
(36) Harel, M.; Taitelbaum, H. Non-monotonic dynamics of thin film spreading. *Eur. Phys. J. E* **2021**, *44*, 69.
(37) Okuzono, T.; Ozawa, K.; Doi, M. Simple model of skin formation caused by solvent evaporation in polymer solutions. *Phys. Rev. Lett.* **2006**, *97*, 136103.
(38) Wodo, O.; Ganapathysubramanian, B. How do evaporating thin films evolve? Unravelling phase-separation mechanisms during solvent-based fabrication of polymer blends. *Appl. Phys. Lett.* **2014**, *105*, 153104.
(39) Kern, W. The evolution of silicon wafer cleaning technology. *J. Electrochem. Soc.* **1990**, *137*, 1887−1892.
(40) Nečas, D.; Klapetek, P. Gwyddion: an open-source software for SPM data analysis. *Open Phys.* **2012**, *10*, 181−188.
(41) Mitchell, J.; Weimer, J. J. Controlled Spreading Rates to Distribute Nanoparticles as Uniform Langmuir Films. *Langmuir* **2021**, *37*, 5139−5150.
(42) Wyart, F. B.; Martin, P.; Redon, C. Liquid/liquid dewetting. *Langmuir* **1993**, *9*, 3682−3690.
(43) Fan, X.; Wang, C.; Fei, L.; Zhou, Q.; Xue, Z.; Ma, J.; Ma, Y. Nascent Holes on Spin-Coated Polymer Nanofilms: Effect of Processing and Solvents. *ACS Appl. Polym. Mater.* **2022**, *4*, 2767−2782.
(44) *Intermolecular and Surface Forces*, 3rd ed.; Israelachvili, J. N., Ed.; Academic Press: San Diego, 2011; pp 661−674.
(45) Sharma, A.; Reiter, G. Instability of thin polymer films on coated substrates: rupture, dewetting, and drop formation. *J. Colloid Interface Sci.* **1996**, *178*, 383−399.
(46) Seemann, R.; Herminghaus, S.; Jacobs, K. Dewetting patterns and molecular forces: A reconciliation. *Phys. Rev. Lett.* **2001**, *86*, 5534−5537.
(47) Shiri, R.; Schmeller, L.; Peschka, D.; Seemann, R.; Wagner, B. Impact of noise on spinodal dewetting of liquid-liquid films. *Commun. Phys.* **2023**, *6*, 109.
(48) Rubinstein, M.; Colby, R. H. *Polymer Physics*; Oxford University Press, 2003.
(49) Meyerhofer, D. Characteristics of resist films produced by spinning. *J. Appl. Phys.* **1978**, *49*, 3993−3997.
(50) Beaucage, G. Approximations leading to a unified exponential/power-law approach to small-angle scattering. *J. Appl. Crystallogr.* **1995**, *28*, 717−728.
(51) Hammouda, B. Analysis of the Beaucage model. *J. Appl. Crystallogr.* **2010**, *43*, 1474−1478.
(52) Diez, J. A.; González, A. G.; Garfinkel, D. A.; Rack, P. D.; McKeown, J. T.; Kondic, L. Simultaneous decomposition and dewetting of nanoscale alloys: A comparison of experiment and theory. *Langmuir* **2021**, *37*, 2575−2585.
(53) Cahn, J. W.; Hilliard, J. E. Free energy of a nonuniform system. I. Interfacial free energy. *J. Chem. Phys.* **1958**, *28*, 258−267.
(54) Cross, M.; Greenside, H. *Pattern Formation and Dynamics in Nonequilibrium Systems*; Cambridge University Press, 2009.
(55) Manzanarez, H.; Mericq, J.; Guenoun, P.; Bouyer, D. Modeling the interplay between solvent evaporation and phase separation dynamics during membrane. *J. Membr. Sci.* **2021**, *620*, 118941.
(56) Thiele, U. Thin film evolution equations from (evaporating) dewetting liquid layers to epitaxial growth. *J. Condens. Matter Phys.* **2010**, *22*, 084019.

https://doi.org/10.1021/acspolymersau.4c00018
ACS Polym. Au 2024, 4, 302−310